SCIENCE CHINA
Information Sciences

• Supplementary File •

Bridging quantum elementary links with spectral steering

Rui-Ming ZHANG[1,2,3], Yun-Ru FAN[1,2,3*], Chen-Zhi YUAN[1,4], Hao YU[1,2,3], Hao LI[5],
You WANG[1,6], Guang-Wei DENG[1,3,7], Hai-Zhi SONG[1,6*], Li-Xing YOU[5],
Guang-Can GUO[1,2,3,7] & Qiang ZHOU[1,2,3,7*]

[1]*Institute of Fundamental and Frontier Sciences, University of Electronic Science and Technology of China,*
Chengdu 611731, China
[2]*Center for Quantum Internet, Tianfu Jiangxi Laboratory, Chengdu 641419, China*
[3]*Key Laboratory of Quantum Physics and Photonic Quantum Information, Ministry of Education,*
University of Electronic Science and Technology of China, Chengdu 611731, China
[4]*Present address: Hubei Key Laboratory of Optical Information and Pattern Recognition,*
Wuhan Institute of Technology, Wuhan 430205, China
[5]*National Key Laboratory of Materials for Integrated Circuits, Shanghai Institute of Microsystem and Information Technology,*
Chinese Academy of Sciences, Shanghai 200050, China
[6]*Southwest Institute of Technical Physics, Chengdu 610041, China*
[7]*CAS Key Laboratory of Quantum Information, University of Science and Technology of China, Hefei 230026, China*

Appendix A Experimental setup for frequency shifter

We prepared time-bin qubits using a continuous-wave (CW) laser (PPCL300, Pure Photonics Corp.) modulated by an arbitrary waveform generator (AWG, 70002A, Tektronix Corp.) at 5 MHz. The laser light was sent into an intensity modulator (IM) to carve out early and/or late temporal modes (40 ps duration, 400 ps separation), depending on the desired qubit. The Z-basis qubits $|\psi\rangle = |e\rangle \,/\, |l\rangle$ were generated by carving out an early or a late time bin. The X-basis qubits $|\psi\rangle = (|e\rangle + e^{i\varphi_0}\,|l\rangle)/\sqrt{2}$ were generated by carving out an early and a late bin of equal intensity, where φ_0 represents the phase difference between two temporal modes. To obtain optical pulses with high extinction ratio, the magnitude of the electrical signal is amplified to match the V_π of the IM (GC15MZPD7813, CETC Corp.) using a microwave amplifier (SHF S126A, SHF Communication Technologies Corp.). A 99:1 BS combined with a photodetector was used for the feedback control loop to ensure that the IM operated under an optimal bias voltage. Then, the dual-pulse signal was sent to a phase modulator (PM, GC15PMTC7813, CETC Corp.), which applied a phase shift of $\varphi_0 = \pi$ to the late mode. Hence, the PM was only activated to generate the states $|-\rangle$. Finally, a variable optical attenuator (VOA) reduced the pulse intensity to the single-photon level.

As shown in Fig. A1(a), the spectrum of time-bin qubits is manipulated by a single-photon frequency shifter (FS), which is implemented using a PM driven by a ramp generator (RG). The RG receives the trigger signal synchronized with the qubits and generates a reversed pulse with a linear high-voltage ramp $V(t) = \kappa t$. The voltage ramp is used as a feedforward signal and is applied to the electrical input of the PM. By carefully adjusting the arrival time, the entire time-bin qubits $|\psi\rangle$ are locked to the linear region of the ramp signal as shown in the inset of Fig. A1(a). We set the duration of the time-bin wave-packet shorter than the ramp signal, in such a way to ensure that only linear phase modulation is applied to the qubits. This modulation induces a linearly varying temporal phase $\Delta\psi(t) = \pi V(t)/V_\pi$ for the time-bin qubits $|\psi\rangle$, which effectively shifts the frequency of the qubits. Meanwhile, the magnitude and polarity of the frequency shift are determined by the slope of the ramp signal.

In the experiment, we select the corresponding rising edge κ_+ and falling edge κ_- of the ramp signal for the frequency shift. Here $\kappa_\pm$ represents the voltage ramp of the pulse edge. The ramp voltage is then sent to the PM, modulating the phase of the single-photon wave packet as follows:

$$\epsilon(x,t) = |\epsilon(x,t)| e^{i2\pi f_0 t + \Delta\psi(t) - ikx} = |\epsilon(x,t)| e^{i2\pi (f_0 + \frac{\kappa_\pm}{2V_\pi})t - ikx}. \tag{A1}$$

where the single-photon wave packet $\epsilon_{in}(x,t) = |\epsilon(x,t)| exp(i2\pi f_0 t - ikx)$ is depicted by the slowly varying envelope approximation, while V_π is the π-voltage of the EOM. The center frequency of the single-photon wave packet is f_0 and its wave vector is k.

Therefore, the magnitude of the frequency shift, f_s (in Hertz), can be expressed as:

$$f_s = \frac{\kappa_\pm}{2V_\pi}. \tag{A2}$$

---

* Corresponding author (email: yunrufan@uestc.edu.cn, hzsong@uestc.edu.cn, zhouqiang@uestc.edu.cn)

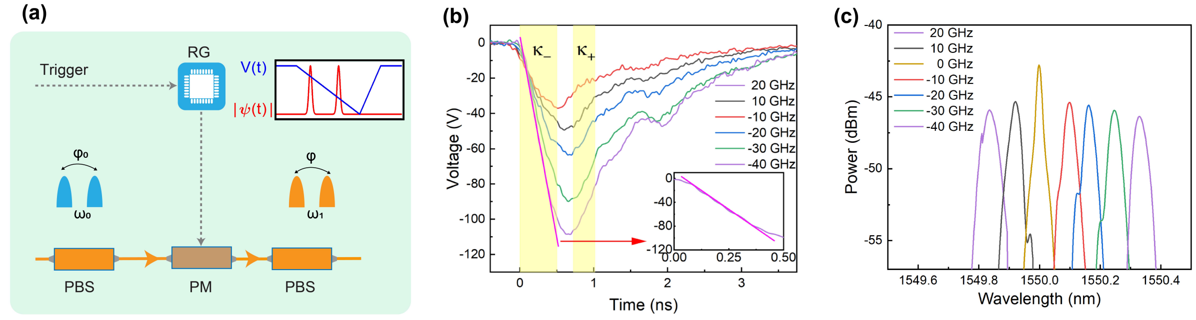

Figure A1 Experimental setup for frequency shifter (FS). (a) Experimental setup for FS based on a phase modulator. Inset: Schematic illustrating a linear temporal phase applied to a time-bin qubit $|\psi\rangle$ (red) synchronized with the ramp phase modulator (PM) driving voltage $V(t)$ (blue). (b) Driver signal for the FS. The shaded part is the linear regimes for frequency shifting at falling edge κ_- and raising edge κ_+. The solid magenta line shows the linear fit of the frequency shift at 40 GHz. The rising/falling edges of the same driving signal (purple) are used at 20 GHz/(-40) GHz. (c) Spectrum output of the FS with frequency shifting for $|e\rangle$ from -40 GHz to 20 GHz.

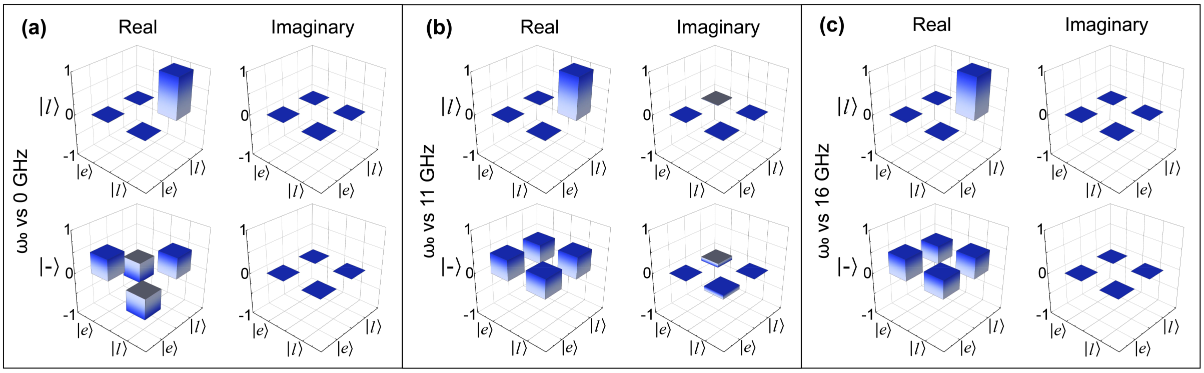

Figure B1 Results of the density matrices. (a), (b) and (c) are the reconstructed density matrices of qubits $|\psi\rangle_B$ at frequency shifts of fs=0 GHz, 11 GHz and 16 GHz, respectively.

The ramp signal for the PM (GC15PMTC9413-LV, CETC Corp.) is generated by our home-built circuit, which is synchronized with the AWG at a repetition rate of 5 MHz. As a master device, the AWG provides synchronization signals to other devices and generates pre-programmed pulse signals to trigger the RG. The pulse signal first passes through the high-speed amplifier and then triggers a high-voltage radio frequency (RF) transistor, resulting in the emission of a reverse pulse with a linear high-voltage ramp. The ramp signal has a voltage as high as 110 V within a fall time of 700 ps as shown in Fig. A1(b). Figure A1(c) presents the spectral output of the frequency-shifted signal for $|e\rangle$. Frequency shifting from -40 GHz to 20 GHz is tested with 10 GHz steps, which is realized by the linear temporal phase modulation of light pulses by the PM. The decrease in the frequency-shifted optical signal in Figure A1(c), is due to the limited extinction ratio of the frequency-shifted optical pulse (27 dB in our setup). Increasing the extinction ratio of the optical pulse can reduce the loss caused by frequency shifting. The ramp signal and the optical signal can be easily stabilized and locked, in such a way to ensure the stability of our frequency shifter. The maximum frequency shifting is 40 GHz, corresponding to a slew-rate of up to 157 V/ns.

Appendix B Quantum state tomography for different frequency shift settings

Using the method in Ref. [1], projection measurements of time-bin qubits are performed via an unbalanced Mach-Zehnder interferometer (UMZI), with the time delay between its arms matching the time-bin interval. By injecting time-bin qubits in the state $|\psi_0\rangle = \alpha\,|e\rangle + \beta\,|l\rangle$ (with $|\alpha|^2 + |\beta|^2 = 1$) into the UMZI, photons are detected in three possible time slots. Detection in the first (third) slot projects onto $|e\rangle$ ($|l\rangle$), while detection in the middle slot projects onto $(|e\rangle + e^{-i\theta}\,|l\rangle)/\sqrt{2}$, where θ is the phase difference between the arms.

In order to obtain the density matrix of the time-bin qubits, we configure the UMZI for each qubit in $|e\rangle$ and $|l\rangle$, $|D\rangle$, and $|R\rangle$, where $|D\rangle = (|e\rangle + |l\rangle)/\sqrt{2}$ and $|R\rangle = (|e\rangle + i\,|l\rangle)/\sqrt{2}$. Meanwhile, we use the $|+\rangle$ of Node A as a reference to ensure that the X-basis states at Node A/B are defined identically. Here, we also present the reconstructed density matrices of $|l\rangle$ and $|-\rangle$ (where $|-\rangle = (|e\rangle - |l\rangle)/\sqrt{2}$) at different frequency shifts of fs=0 GHz (the FS is turned off), 11 GHz, and 16 GHz, respectively. Fig. B1 shows the reconstructed density matrix of the quantum states of $|l\rangle$ and $|-\rangle$. For fs=11 GHz, the fidelities between the qubits before and after frequency shifting are 99.71±0.03% and 18.87±0.17% for $|l\rangle$ and $|-\rangle$, respectively. For fs=16 GHz, the fidelities between the qubits before and after frequency shifting are 99.98±0.04% and 99.11±0.01% for $|l\rangle$ and $|-\rangle$, respectively.

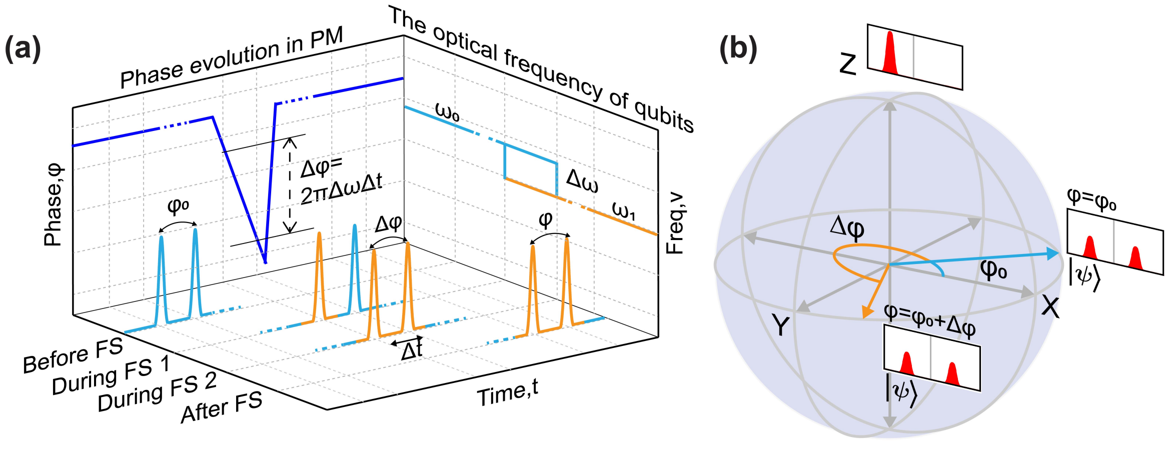

Figure C1 Conceptual illustration of the quantum state evolution caused by FS. (a) Optical frequency of time-bin qubits during frequency shifting with a Δt time interval. To illustrate the evolution during the frequency shifting, the phase in the PM is taken as a reference (blue line), which is consistency with the trend of the ramp signal. The frequency variations, corresponding to different moments of phase evolution, are illustrated using different colors. The left photon wave packets correspond to the earlier time bin. (b) Phase evolution of time-bin qubits on the Bloch sphere.

Appendix C Quantum state evolution caused by single-photon frequency shifter

In our work, the utilization of a FS based on a phase modulator will inevitably lead to an additional phase shift for time-bin qubits [2]. An intuitive picture helps us to understand how the phase and frequency evolve during the frequency shifting, as shown in Fig. C1(a). We consider the prepared $|\psi\rangle$ with a central frequency of f_0 and a relative phase of φ_0 between the early and late bin (labeled as Before FS in Fig. C1(a)). When the early bin passes through the PM driven by a ramp signal, the frequency shift of fs is introduced (labeled as During FS 1). Similarly, when the late bin encounters the ramp signal on the phase modulator, an identical fs frequency shift occurs (labeled as During FS 2), assuming the ramp has the same voltage slope. However, the accumulation of time changes the voltage applied to the PM ($\Delta V = \kappa_{\pm}\Delta t = 2V_{\pi} fs \Delta t$), thus alters the phase of the late bin and creates a phase difference $\Delta\varphi$ between two temporal modes:

$$\Delta\varphi = \frac{\Delta V}{V_{\pi}}\pi = 2\pi fs \Delta t. \tag{C1}$$

Here, Δt is the time-bin spacing of the qubits. After the frequency shift (labeled as After FS), the qubit frequency within the temporal aperture defined by the ramp signal is shifted, and the phase difference $\Delta\varphi$ is also preserved. With our experiment setup, Δt and fs need to be chosen to maintain high fidelity such that $\Delta t * fs = k$, where k is an integer.

The qubit evolution of the FS can be illustrated as two different points on the surface of the Bloch sphere, as shown in Fig. C1(b). The equatorial qubits X and Y correspond to two pulses of equal intensity with a phase difference of φ_0, where the quantum information is encoded by the phase (φ_0). The polar coordinate basis Z corresponds to pulses in one of the two time-bins. When the quantum state passes through the FS based on the PM, the frequency shift fs of the time-bin qubits $|\psi\rangle$ come along with a rotation of an angle $\Delta\varphi$ in the equatorial plane, which could introduce bit errors in the qubit decoding. In constrast, the Z-basis can be decoded by measuring the arrival time of the time-bins in the receiver detectors. Therefore, the Z-basis is phase independent, and the fidelities of Z-basis are maintained after the frequency shifting.

Appendix D Bounding the single photon fidelity of BSM using decoy state analysis

Decoy state analysis allows the implementation of quantum key distribution protocols using attenuated laser pulses while providing immunity against the photon number splitting attacks [3, 4] and allows estimating the final key stems only from states containing one photon. The application of this analysis can be further generalized to allow any experiment performed with weak coherent states, i.e., attenuated laser pulses, to mimic an experiment using a much more elaborate setup that incorporates single photon (Fock) states. It has been extended to verify the quantum nature of memory [2] and teleportation [5, 6], which provides avenues for simpler experimental demonstrations of complex protocols. Here we use decoy state analysis to prove the quantum nature of Bell state measurement (BSM) [7] and provide a brief outline of how it is employed in our experiment. This requires announcing the events for which the measurement resulted in a projection onto the $|\psi^{-}\rangle$ state, provided that these states are encoded into individual photons. The BSM fidelity can be estimated from the probabilities of correct output (P_c) and false output (P_f) [8] as follows:

$$F = \frac{P_c}{P_c + P_f}. \tag{D1}$$

where F represents the fraction of correct labels among all unambiguous results, ranging from 0 (all incorrect) to 1 (all correct).

First, we define the error rate:

$$E = \frac{C_{\psi_\perp|\psi}}{C_{\psi_\perp|\psi} + C_{\psi|\psi}}. \tag{D2}$$

where, $C_{\psi_\perp|\psi}$ denotes the number of measured events corresponding to the state $|\psi_\perp\rangle$, while the expected state is $|\psi\rangle$. Since $|\psi_\perp\rangle$ is orthogonal to $|\psi\rangle$, a photon count of $|\psi_\perp\rangle$ constitutes an error. Compared to the expression for the fidelity, it is clear that *F=1-E.*

We use the three-intensity decoy state approach for BSM, in such a way to calculate a lower bound of the fidelity. For Node A/B, we denote the signal, decoy, and vacuum state by μ_s, μ_d, and μ_v, respectively (note that, by definition, $\mu_v = 0$). In our implementation, both Node A and B choose the same average number of photons for the three intensities, and use identical transmitted channels. For notational brevity, we omit μ when describing yield and error rate (e.g. $Q^{x,z}_{i,j}$ is the corresponding gain when the Node A/B prepare qubits in X, Z-basis with mean photon number $\mu_i(\mu_j)$. We write Q^z_{ss} to denote gain in Z basis when both Node A and B send photons using signal state). Under these assumptions, the lower bound of Q^x_{11} is given by:

$$Q^x_{11} \geqslant \frac{P_1(\mu_s)P_2(\mu_s)(Q^x_{dd} - Q^x_0(\mu_d)) - P_1(\mu_d)P_2(\mu_d)(Q^x_{ss} - Q^x_0(\mu_s))}{P_1(\mu_s)P_1(\mu_d)(P_1(\mu_d)P_2(\mu_s) - P_1(\mu_s)P_2(\mu_d))}. \tag{D3}$$

where the various $P_i(\mu)$ denote the probabilities that a pulse with Poissonian photon number distribution and mean μ contains exactly i photons, and $Q^x_0(\mu_d)$ and $Q^x_0(\mu_s)$ are given by:

$$Q^x_0(\mu_d) = P_0(\mu_d)Q^x_{vd} + P_0(\mu_d)Q^x_{dv} - P_0(\mu_d)^2 Q^x_{vv}. \tag{D4}$$

$$Q^x_0(\mu_s) = P_0(\mu_s)Q^x_{vs} + P_0(\mu_s)Q^x_{sv} - P_0(\mu_s)^2 Q^x_{vv}. \tag{D5}$$

Based on table 2 from Ref. [9], the error rate for the single photon component in a coherent pulse is upper bounded by e^x_{11}, which is:

$$e^x_{11} \leqslant \frac{e^X_{dd}Q^x_{dd} - P_0(\mu_d)e^x_{vd}Q^x_{vd} - P_0(\mu_d)e^x_{dv}Q^x_{dv} + P_0(\mu_d)^2 e^x_{vv}Q^x_{vv}}{P_1(\mu_d)^2 Q^x_{11}}. \tag{D6}$$

where the upper bound holds if a lower bound is used for Q^x_{11}. Note that $Q^{x,z}_{11}$, $Q^{x,z}_0(\mu_d)$, $Q^{x,z}_0(\mu_s)$ and $e^x_{11}(\mu_d)$ are uniquely determined through measurable gains and error rates. Here, μ_d is the mean photon number per qubit encoded into a decoy state; $Q(\mu_d)$ is the corresponding gain (i.e. the probability for a 3-fold coincidence when creating pulses with mean photon number μ_d at Node A), and $e(\mu_d)$ is the corresponding error rate; *e(0)* is the error rate for a zero-photon (vacuum) input at Node A; *Y(0)* and $Y_0(1)$ are the yield for a zero-photon input and the lower bound for the yield of a single photon input, respectively. The values $Q(\mu_d)$, $e(\mu_d)$, *Y(0)* and *e(0)* can be measured directly in the experiment. Thus, we can calculate an upper bound of the error rate $E^{(1)}_U$. In turn, this allows computing a lower bound on the fidelity in the BSM between adjacent elementary links:

$$F^{(1)} = 1 - E^{(1)} \geqslant 1 - E^{(1)}_U \equiv F^{(1)}_L. \tag{D7}$$

which thus allows us to calculate the values in Table 1 in the main text.

Appendix E Spectrally multiplexed BSM for MDI-QKD

We characterize the performance of our spectrally multiplexed BSM by calculating the secret key rate of the spectrally multiplexed measurement-device-independent quantum key distribution (MDI-QKD). The time-bin qubits are characterized following the procedure described in [10]. Motivated by our setups, which create imperfect pure states, we consider time-bin qubits of the form:

$$|\varphi\rangle = \frac{1}{\sqrt{1+2b^{x,z}}}(\sqrt{m^{x,z}+b^{x,z}}\,|e\rangle + e^{i\theta^{x,z}}\sqrt{1-m^{x,z}+b^{x,z}}\,|l\rangle). \tag{E1}$$

Where, $m^{x,z} = \frac{S^{x,z}_e}{S^{x,z}_e + S^{x,z}_l}$, and $b^{x,z} = \frac{B}{S^{x,z}_e + S^{x,z}_l}$. Furthermore, the superscript indicates to which basis/state the parameter applies (for example m^z=0 applies to the state produced when Node A/B chooses the Z-basis state $|l\rangle$). For perfect time-bin qubits preparation setup, m$^{(z=0,1)}$=0 or 1 for qubits in the Z-basis, and m$^{(x=+,-)}$=0.5 for qubits in the X-basis; $\theta^{(x,z)}$=0 or π for qubits in the X-basis (in the Z-basis θ^z is irrelevant) and $b^{(x,z)}$ would be zero. The experimentally determined parameters $S^{x,z}_{e,l}$ and B are established independently for each pair of qubits belonging to a mutually unbiased basis, as depicted in Fig. E1 for states $|e\rangle$ and $|+\rangle$. These parameters were measured for both implementations, and the results are given in Table E1.

Based on the modeled factors such as loss and observed Hong-Ou-Mandel (HOM) dip visibility [10], we can simulate the secure key rate of the MDI-QKD as shown in Fig. E2. To assess the potential impact of the proposed spectrally multiplexed BSM, we calculate the secret key rates for three different scenarios: (1) the current experimental scenario without FS for a single-mode BSM; (2) the current experimental conditions with spectral multiplexing; and (3) the state-of-the-art integrated lithium niobate PM from [11] to perform frequency shifting.

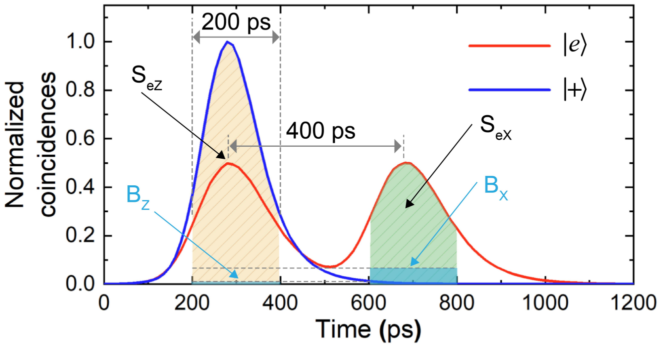

Figure E1 Set of experimentally measured parameters that constitute the inputs for the key rate estimation model. Highlighted zones are $S_{e,l}^{x,z}$ and B for bases Z and X respectively.

Table E1 Experimentally established values for all parameters required to describe the generated quantum states, as well as HOM interference parameters and detector properties.

Parameter	Value
$\mathrm{b}^{z=0}=\mathrm{b}^{z=1}$	4.74×10^{-4}
$\mathrm{b}^{x=+}=\mathrm{b}^{x=-}$	0.0556
$\mathrm{m}^{z=0}$	0.9995
$\mathrm{m}^{z=1}$	0
$\mathrm{m}^{x=+}=\mathrm{m}^{x=-}$	0.4961
$\theta^{z=0}=\theta^{z=1}=\theta^{x=+}$	0
$\theta^{x=-}$	$\pi\pm0.075$
$\lvert\theta_{freq}\rvert$ $[rad]$	< 0.38
V	< 0.43
P_d	6×10^{-8}
η	0.84

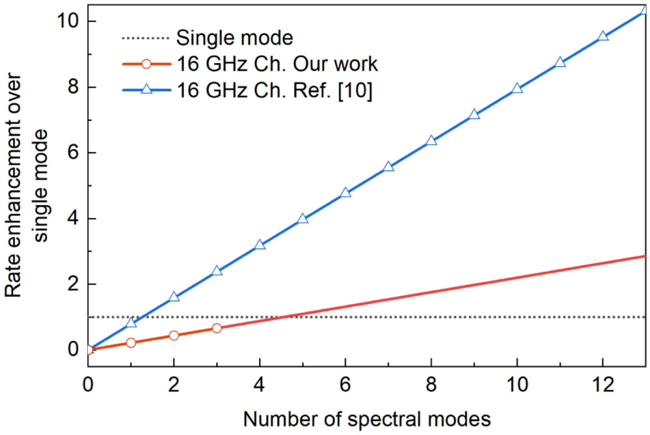

Figure E2 Secret key rate of the MDI-QKD. Enhancement of the secret key rate over the single-mode case for different numbers of spectral modes assuming two different experimental conditions. "Ref. [11]" and "Our work" denote the state-of-the-art integrated lithium niobate PM and the current experimental scenarios used component PM, respectively. The gray dotted line represents the single-mode case without frequency shifting.

The key rate for a single mode is shown as a reference (gray dotted line) where only one spectral mode is used to perform the BSM. Our analysis is based on the current wavelength channel assignment with a frequency interval of 16 GHz (red circle). The FS is realized by a PM with a half-wave voltage of 2.3 V and an insertion loss of 3.8 dB, respectively. With our setup, three-channel multiplexing can achieve 60% of the rate compared with the single-mode BSM case, and the proposed spectrally multiplexed BSM outperforms single-mode BSMs when employing more than five spectrally multiplexed channels. Assuming the FS is built with the integrated lithium niobate PMs with a half-wave voltage of 1.4 V and an insertion loss of 0.5 dB [11], it is possible to multiplex 13 spectral modes within a bandwidth of 200 GHz, resulting in an improvement of more than 10 times (as shown in the blue curve). The rate enhancement can be realized when employing more than two spectrally multiplexed channels, compared with the case without spectral multiplexing.

References

1 James D F, Kwiat P G, Munro W J, et al. Measurement of qubits. Physical Review A, 2001, 64: 052312
2 Sinclair N, Saglamyurek E, Mallahzadeh H, et al. Spectral multiplexing for scalable quantum photonics using an atomic frequency comb quantum memory and feed-forward control. Physical Review Letters, 2014, 113: 053603
3 Dušek M, Haderka O, Hendrych M. Generalized beam-splitting attack in quantum cryptography with dim coherent states. Optics Communications, 1999, 169: 103–108
4 Brassard G, Lütkenhaus N, Mor T, et al. Limitations on practical quantum cryptography. Physical Review Letters, 2000, 85: 1330
5 Shen S, Yuan C, Zhang Z, et al. Hertz-rate metropolitan quantum teleportation. Light: Science & Applications, 2023, 12: 115
6 Valivarthi R, Puigibert M l G, Zhou Q, et al. Quantum teleportation across a metropolitan fibre network. Nature Photonics, 2016, 10: 676–680
7 Wang X B. Three-intensity decoy-state method for device-independent quantum key distribution with basis-dependent errors. Physical Review A, 2013, 87: 012320
8 Bayerbach M J, D'Aurelio S E, Van Loock P, et al. Bell-state measurement exceeding 50% success probability with linear optics. Science Advances, 2023, 9: eadf4080
9 Xu F, Curty M, Qi B, et al. Practical aspects of measurement-device-independent quantum key distribution. New Journal of Physics, 2013, 15: 113007
10 Chan P, Slater J A, Lucio-Martinez I, et al. Modeling a measurement-device-independent quantum key distribution system. Optics Express, 2014, 22: 12716–12736
11 Hu Y, Yu M, Zhu D, et al. On-chip electro-optic frequency shifters and beam splitters. Nature, 2021, 599: 587–593